Title

Vetting of 384 TESS Objects of Interest with TRICERATOPS and Statistical Validation of 12 Planet Candidates

Journal

Astronomical Journal, 161(1)

ISSN

0004-6256

Authors

Giacalone, S
Dressing, CD
Jensen, ELN
et al.

Publication Date

2021

DOI

10.3847/1538-3881/abc6af

Peer reviewed

Draft version February 4, 2020
Typeset using LaTeX **twocolumn** style in AASTeX63

`triceratops`: A Tool for Rapid Validation of *TESS* Objects of Interest and Application to 424 Planet Candidates

Steven Giacalone[1] and Courtney D. Dressing[1]

[1]*Department of Astronomy, University of California Berkeley, Berkeley, CA 94720-3411, USA*

Submitted to AAS journals

ABSTRACT

We present a new tool, `triceratops`, that can be used to rapidly validate *TESS* Objects of Interest (TOIs). We test this procedure on 213 TOIs that have been previously confirmed as planets or rejected as astrophysical false positives. We find that our tool is generally able to distinguish bona fide planets from astrophysical false positives for TOIs with radii smaller than $8R_{\oplus}$, and that it performs better when the candidate host is observed with a shorter cadence. We apply this procedure on 424 unclassified TOIs and identify 262 that have high probabilities of being bona fide planets and 61 that have high probabilities of being false positives. We discuss how this tool can be utilized for follow-up target prioritization and how it can be used in tandem with existing vetting tools to perform thorough validation analyses of planet candidates detected by *TESS*.

1. INTRODUCTION

Over the last decade, the *Kepler* Space Telescope has revolutionized our understanding of exoplanets by facilitating the discovery of thousands of planets that transit in front of their host stars. Among other things, these planets have been useful for investigating the frequency of planets as a function of size and orbital period (e.g., Howard et al. 2012; Dong & Zhu 2013; Dressing & Charbonneau 2013; Fressin et al. 2013; Petigura et al. 2013; Sanchis-Ojeda et al. 2014; Burke et al. 2015; Dressing & Charbonneau 2015; Mulders et al. 2015a,b; Fulton et al. 2017), as well as testing theories of planet formation and evolution (e.g., Lopez & Fortney 2013; Lee & Chiang 2017; Königl et al. 2017; Giacalone et al. 2017). To ensure the veracity of their results, studies that utilized the *Kepler* dataset required that: (1) the measured radii of these planets were accurate, and (2) that the discovered objects were actually planets. However, due to the limited $4''$ resolution of the camera used by *Kepler*, these two requirements could not always be assumed true. Unless the field of stars within a given pixel was known to a higher precision than this resolution, the possibility of a star other than the target star existing within that pixel could not be discounted. This uncertainty was problematic because it could cause an underestimation of the radius of a transiting object within the pixel, sometimes to the extent that an eclipsing binary star could be mistaken for a transiting planet with a fraction of the size.

A number of methods have been used to constrain the possibility of an unresolved star residing within a given pixel. One method used is to search for shifts in the centroid of the source during transit, a signal indicative of another star residing elsewhere in the pixel (Coughlin et al. 2014). Multi-band time-series photometry has also been used to search for unresolved stars, as one would expect a different transit depth in different photometric bands if the transiting object is around a star of a different color than the target (e.g., Alonso et al. 2004). Spectra of the target star can also be useful in this vetting process. High-precision radial velocities can rule out bound stellar companions by measuring the masses of transiting objects and monitoring for longer-period secondaries (e.g., Errmann et al. 2014), and reconnaissance spectroscopy can rule out bright unresolved stars by searching for additional lines in the spectrum of the target star (e.g., Santerne et al. 2012). Finally, high-resolution imaging can rule out unresolved stars beyond a fraction of an arcsecond from the target star (e.g., Crossfield et al. 2016). Unfortunately, these techniques do not cover the full allowed parameter space individually, and *Kepler* planet candidate hosts were often too faint to obtain precise radial velocity measurements of from the ground. For this reason, it was common to turn

Corresponding author: Steven Giacalone
steven_giacalone@berkeley.edu

to validation to assess the genuineness of *Kepler* planet candidates.

Validation is the process of statistically arguing that a transit-like signal is due to a planet rather than an astrophysical false positive, like an eclipsing binary star that is blended within a common pixel, given the light curve and any external information about the host star. A number of validation algorithms were used during the *Kepler* era for the purpose of identifying the planetary candidates with the highest chances of being bona fide planets in order to grow the dataset with which large-scale studies of planetary system properties could be conducted.

The first *Kepler*-era validation framework was `blender` (Torres et al. 2004, 2005, 2010b). `blender` operates by generating synthetic light curves and multi-band photometry for a multitude of false positive scenarios over a wide parameter space. `blender` then rules out false positive scenarios by comparing the shapes of the synthetic transits with the shape of the actual *Kepler* light curve and comparing the synthetic photometry with actual photometric observations of the target both in and out of transit. The first of these comparisons is done because the shape of a transit is tied to the size of the transiting object relative to the host star, and can thus help distinguish transits that are caused by star-sized objects from those caused by planet-sized objects. The second comparison is done because, for a pair of stars where each star is of a different spectral type, the observed color of the target will change as the secondary obscures some of the light from the primary. This constraint can therefore be used to differentiate transits that come from eclipsing binary stars from those that come from transiting planets. In addition to these metrics, `blender` can also fold in high resolution imaging data, spectroscopic measurements, and centroid position variations to obtain an even tighter constraint on the range of possible false positive scenarios.

`blender` offered the most thorough option for the validation of transiting planet candidates during the *Kepler* era. However, the long computation times required to simulate the many false positive scenarios involved in its analysis made it inefficient for validating planet candidates in bulk. This led to the formulation of a different validation procedure by the name of `vespa` (Morton 2012, 2015). `vespa` provides a more computationally expedient option for validating planet candidates by replacing the full transit models employed in `blender` with a simpler trapezoidal model, which can capture the most important features of the transit shape with fewer free parameters.

`vespa` works in a Bayesian framework where priors and likelihoods of several false positive scenarios are compared to those of a transiting planet scenario to compute an effective probability that the latter is true. For every scenario, `vespa` uses the TRILEGAL galactic model (Girardi et al. 2005) to simulate a population of stars with properties consistent with the target star in a cone around the line of sight to the target. In cases where the properties of the target star are not well-constrained, they are estimated using archival photometry and isochrone interpolation. These simulated populations are used in tandem with assumptions relating to stellar mutliplicity and planet occurrence rates to calculate the prior probability and distribution of possible transit shapes for the scenario. `vespa` then uses a Markov Chain Monte Carlo (MCMC) routine to fit the *Kepler* light curve of the target to a trapezoidal model and calculates the likelihood for every scenario by comparing the best-fit transit shape to their transit shape distributions. Lastly, the probability of the transiting planet scenario is assessed by comparing the product of the prior and likelihood for the transiting planet scenario with those of all of the false positive scenarios considered. Like `blender`, `vespa` can also incorporate follow-up observations, such as high resolution imaging, to improve the accuracy of its procedure.

Another procedure used to validate exoplanet candidates is `pastis` (Díaz et al. 2014; Santerne et al. 2015). `pastis` provides a rigorous option for the validation of small planetary transits by calculating the Bayesian odds ratio between the transiting planet scenario and all possible false positive scenarios for a given target star. Priors are computed for each scenario by combining information about the target, including that contained within ground-based follow-up observations, with knowledge of stellar multiplicity and planet occurrence rates. In addition, for false positive scenarios that involve an unresolved foreground or background star, TRILEGAL is used to simulate a population of stars around the line of sight to target to calculate the prior probability of such a chance alignment. Likelihoods are determined using a MCMC algorithm that samples the posterior parameter distribution of each scenario. In addition to modeling the radial velocities of its targets, `pastis` uses full light curve models in its analysis, rather than using the trapezoidal simplification employed by `vespa`. Like those utilized with `blender`, these light curve models are dependent on more free parameters than the trapezoidal model, meaning `pastis` must sample over a wider parameter space when computing the likelihood of each scenario. While ensuring that all possible parameter combinations for each scenario are con-

sidered, this method requires significantly more time to run for a given target than `vespa` does.

Each of the aforementioned validation procedures was designed to work with minimal information about a given target star in order to argue for the existence of a transiting planet around it. This design mainly grew out of necessity, as information about many planet candidate hosts and the region of sky in which they were located was sparse in the absence of additional observations. For instance, the number of stars within each pixel was often unknown, and the stars that were known were not always precisely characterized. These facts imposed limitations on the functionalities of the procedures. Specifically, it restricted testable false positive scenarios to those involving the target star and a single unresolved star, even though there could have been a multitude of unknown stars in the group of pixels used to extract a given light curve. Additionally, poorly characterized target stars forced these procedures to use stellar models and isochrone interpolation to estimate host star properties, which comes at the cost of both computation time and reliability.

These design features make previous validation algorithms poorly optimized for use on planet candidates identified by the Transiting Exoplanet Survey Satellite (TESS, Ricker et al. 2010). *TESS* differs from *Kepler* by being an all-sky survey that focuses on the nearest and brightest stars in order to find planets that are well-suited for mass measurement and atmospheric characterization. However, this increased sky coverage comes at the cost of resolution. The *TESS* cameras contain pixels that span $21''$, which means each pixel covers an area of sky roughly $25\times$ larger than those utilized by *Kepler* . Because of this, the assumption that there is at most one additional star blended within a given pixel is unlikely to be true. In addition to scenarios involving a bound stellar companion or a chance alignment of a non-associated star near the target star, a *TESS* validation procedure must be capable of considering false positive scenarios around a multitude of stars scattered throughout a given aperture.[1]

Luckily, the drawback of decreased resolution is counteracted by the wealth of information on nearby stars provided by the second *Gaia* data release (DR2, Brown et al. 2018). DR2 provides optical photometry, astrometry, and positions for over one billion of the nearest stars in the Galaxy. Perhaps most importantly, it is reported that DR2 consistently resolves individual point sources that reside more than $2''.2$ apart, which allows for the identification of stars blended within a *TESS* pixel to levels previously only possible with supplementary follow-up. With this knowledge, one can test for false positive scenarios around known nearby stars and conduct more precise centroid analyses. In addition, the focus on nearby and bright stars means that most *TESS* planet candidate hosts can be more easily characterized using archival and follow-up data. In fact, the properties of millions of *TESS* targets have already been compiled in the *TESS* Input Catalog (TIC, Stassun et al. 2018). A validation procedure for *TESS* planet candidates should be designed to leverage these known stellar properties, rather than use stellar models to estimate them.

In this work, we present `triceratops` (**T**ool for **R**ating **I**nteresting **C**andidate **E**xoplanets and **R**eliability **A**nalysis of **T**ransits **O**riginating from **P**roximate **S**tars), a new tool formulated to validate *TESS* planet candidates.[2] The procedure calculates the probabilities of a wide range of transit-producing scenarios using the primary transit of the planet candidate and preexisting knowledge of its host and nearby stars. Moreover, we utilize the known properties of these stars to calculate star-specific priors for each scenario with up-to-date estimates of stellar multiplicity and planet occurrence rates.

Our tool is designed to provide fast[3] and accurate calculations that can be used to not only validate transiting planet candidates, as validation tools have been used to do in the past, but also to serve as a metric for ranking targets of ground-based follow-up programs. Because a majority of *TESS* targets will be bright enough to be followed up with ground-based telescopes, there will inevitably be more planet candidates hosts to observe from the ground than time and resources allow for. We therefore encourage the use of our tool to identify targets that would benefit most from additional vetting.

The layout of this paper is as follows. In Section 2 we present out validation procedure, including how we determine the possible scenarios for a given target star and calculate the probability of each. In Section 3 we present detailed validation results for a previously-confirmed TOIs, as an example. In Section 4 we present the results of validation calculations for a sample of TOIs and an performance assessment. In Section 5 we

[1] It should be noted that because *TESS* focuses on brighter stars than *Kepler* did and the field density of brighter stars is low compared to the field density of fainter stars, most of these contaminating stars will contribute only a small fraction of the total flux within the pixel. By contrast, stars blended within a *Kepler* pixel had a higher probability of having comparable brightnesses.

[2] Available at https://github.com/stevengiacalone/triceratops.

[3] Typical run time of 2 minutes on a standard 2-core laptop.

Table 1. Transit Scenarios

Scenario Name	Unresolved Stellar Companion	Host Star	Parameter Vector, θ_j
TTP	None	Target	(R_p, i)
TEB	None	Target	($f_{\rm EB}$, i)
PTP	Bound	Target	(R_p, i, $f_{\rm c}$)
PEB	Bound	Target	($f_{\rm EB}$, i, $f_{\rm c}$)
STP	Bound	Companion	(R_p, i, $f_{\rm c}$)
SEB	Bound	Companion	($f_{\rm EB}$, i, $f_{\rm c}$)
DTP	Unbound	Target	(R_p, i, $f_{\rm c}$)
DEB	Unbound	Target	($f_{\rm EB}$, i, $f_{\rm c}$)
BTP	Unbound	Companion	(R_p, i, $f_{\rm c}$, $T_{\rm eff,back}$)
BEB	Unbound	Companion	($f_{\rm EB}$, i, $f_{\rm c}$, $T_{\rm eff,back}$)
NTP	None	Nearby Star	(R_p, i)
NEB	None	Nearby Star	($f_{\rm EB}$, i)

apply our tool to 424 unclassified TOIs and identify 262 that have high probabilities of being bona fide planets and 61 that have high probabilities of being astrophysical false positives. In Section 6 we provide a discussion of our results, provide suggestions for how our tool can best be utilized, and present features that we plan on implementing in the future. Lastly, we provide concluding remarks in Section 7.

2. PROCEDURE

Our validation procedure is initiated by selecting a target star listed in the *TESS* Input Catalog (TIC) with a transiting planet candidate. Using the MAST module of `astroquery` (Ginsburg et al. 2019), we query the TIC for all stars within a user-dsignated distance of the target. Next, an aperture is drawn around the pixels surrounding the target (e.g., the aperture used to extract the *TESS* light curve). The positions, *TESS* magnitudes, and available stellar properties of each star within the aperture are recorded for later use. The remaining steps of the procedure are summarized as follows:

1. Calculate the proportion of flux contributed by each star in the aperture to identify the stars bright enough to produce the observed transit-like signal.

2. Using the primary transit of the planet candidate and light curve models of transiting planets and eclipsing binaries, determine the size of the transiting object that maximizes the likelihood of each scenario.

3. Given the properties of the host star, the orbital period of the planet candidate, and the best-fit radius of the transiting object, calculate the prior probability of each scenario.

4. Use these likelihoods and priors to calculate the relative posterior probability of each scenario.

2.1. *Flux Ratio Calculation*

Initially, each star in the aperture is considered a potential origin of the transit-like event. These stars are all contributing different amounts of light to the aperture, and therefore the size that the transiting object must be to produce the observed transit depth is different for each star. That is, a fainter star needs to be eclipsed by a larger object than a brighter star when looking at a light curve extracted from the sum of their fluxes. Because the transiting object size is important for determining the probability of each scenario, the relative flux contributed by each star in the aperture is essential information.

We use the *TESS* magnitudes (T) listed in the TIC to estimate the ratio of flux contributed by each star. We identify the brightest object in the aperture and denote its magnitude as $T_{\rm min}$. For each star s, we calculate the relative flux of each star as

$$F_{{\rm rel},s} = 10^{(T_{\rm min} - T_s)/2.5}. \quad (1)$$

The flux ratio of each star is then

$$X_s = \frac{F_{{\rm rel},s}}{\sum_s F_{{\rm rel},s}}. \quad (2)$$

We find that this method produces flux ratios close to the contamination ratios reported for candidate target stars in the TIC (Stassun et al. 2018).

After flux ratios are determined, we eliminate stars that are too faint to produce the observed transit depth. If the observed transit depth is $\delta_{\rm obs}$, the respective transit depth for each star is simply $\delta_s = \delta_{\rm obs}/X_s$. For stars that contribute relatively little flux to the aperture, it is

possible for δ_s to exceed unity. We exclude these stars from further analysis.

2.2. *Transit Scenarios*

After calculating the flux ratio for each star in the aperture, we determine the scenarios within the aperture that can produce the observed transit-like event. Our procedure considers a total of ten scenarios for the target star and an additional two scenarios for every other star in the aperture with $\delta_s < 1$, half of which are transiting planet (TP) scenarios and the other half of which are eclipsing binary (EB) scenarios. These scenarios are summarized in Table 1.

The ten target star scenarios can be classified into three configurations. The first is the case where the target star has no unresolved stellar companion of significant flux (where we define "companion" to encompass both bound and unbound stars). In this case, we consider the scenarios of a TP around the target star (Target TP, or TTP) and an EB around the target star (Target EB, or TEB). The second configuration is that in which there is an unresolved bound stellar companion near the target star. In this case, we consider the scenarios of a TP around the target star (Primary TP, or PTP), an EB around the target star (Primary EB, or PEB), a TP around the companion (Secondary TP, or STP), and an EB around the companion (Secondary EB, or SEB).[4] The third configuration is that in which there there is an unresolved unbound stellar companion in the foreground or background along the line of sight to the target star. In this case, we again consider the scenarios of a TP around the target star (Diluted TP, or DTP), an EB around the target star (Diluted EB, or DEB), a TP around the companion (Background TP, or BTP), and an EB around the companion (Background EB, or BEB).[5]

For stars other than the target star with $\delta_s < 1$, we also consider the scenarios of a TP around that star (Nearby TP, or NTP) and an EB around that star (Nearby EB, or NEB) under the assumption that it has no unresolved stellar companion.

2.3. *Stellar Property Estimation*

Whenever possible, we use the stellar properties listed in the TIC in our validation procedure. However, for reasons that will be discussed, there are times in our procedure where we must estimate the properties (i.e., mass M_*, radius R_*, effective temperature $T_{\rm eff}$, surface gravity $\log g$, and luminosity L_*) of a potential host star in order to determine the probability of the corresponding scenario. We do so using the empirical and semi-empirical relations between stellar properties used to populate these fields in the TIC.

Table 2. Stellar Property Spline Nodal Points

$T_{\rm eff}$ (K)	$M_\star$ ($M_\odot$)	$R_\star$ ($R_\odot$)
42000	40.0	11.0
30000	15.0	6.2
15200	4.4	3.0
11400	3.0	2.6
9790	2.5	2.4
8180	2.0	2.1
7300	1.65	1.8
6650	1.4	1.55
5940	1.085	1.2
5560	0.98	1.05
5150	0.87	0.9
4410	0.69	0.72
4000	0.63	0.64
3800	0.58	0.58
3600	0.48	0.49
3400	0.35	0.35
3200	0.2	0.23
3000	0.135	0.17
2800	0.1	0.1

For stars with $T_{\rm eff} > 4000$ K, we determine stellar properties using the results from Torres et al. (2010a). Using the same method discussed in Section 3 of Stassun et al. (2018), we draw spline curves through the distribution of points in $M_* - T_{\rm eff}$ and $R_* - T_{\rm eff}$ space. For stars with $T_{\rm eff} \leq 4000$ K, we repeat this process using a sample of stars from the specially curated *TESS* Cool dwarf Catalog (Muirhead et al. 2018). We select nodal points using the sample such that they are continuous with the curves obtained for hotter stars.

The aforementioned nodal points are shown in Table 2. Using these, we calculate analogous curves in $\log g - T_{\rm eff}$ and $L_* - T_{\rm eff}$ space. The result of this process is a set of relations that, given a value for one of these properties, allows us to estimate the values of the other four.

In the event that a star does not have any of these five properties characterized, we estimate $T_{\rm eff}$ in the same way outlined in Section 2.2.4 of Stassun et al. (2018), which makes use of V and K_s magnitudes and color-temperature relations from Casagrande et al. (2008) and Huang et al. (2015). Assuming the star is on the main se-

[4] The PEB and SEB scenarios have also been referred to as Hierarchical EBs, or HEBs, in the literature.

[5] The BTP and BEB scenarios also include unresolved foreground stars, but the case where a background star is blended with the target star is typically the relevant one.

quence, we then use the spline relations described above to estimate the remaining properties.

2.4. *Probabilistic Framework*

We employ a Bayesian framework in our validation of planetary transits, and thus make use of Bayes' theorem:

$$p(S_j|D) \propto p(S_j)p(D|S_j) \tag{3}$$

where $p(S_j|D)$ is the posterior probability of the jth scenario S_j given the data D, $p(S_j)$ is the prior probability of scenario S_j, and $p(D|S_j)$ is the global likelihood of the data D given the scenario S_j. When working with a model characterized by the parameter vector θ_j, the global likelihood is often expressed as the marginalization of the likelihood $p(D|\theta_j, S_j)$ over θ_j:

$$p(D|S_j) = \int p(\theta_j|S_j)p(D|\theta_j, S_j)d\theta \tag{4}$$

where $p(\theta_j|S_j)$ is the prior distribution of the model parameters. Because this integral is typically impossible to solve analytically, it is common to approximate the integral by sampling $p(\theta_j|S_j)$. This is, in fact, the method done when calculating odds ratios between competing scenarios in the `pastis` validation procedure. While robust, this method can be computationally costly when sampling a high-dimensional parameter space. In order to provide fast probabilities for each transit scenario, we makes a few simplifications to this approach.

First, we reduce the number of free parameters in θ_j using information in the TIC. Light curve models for TPs and EBs require the properties of the host star, the properties of the transiting object, and the orbital parameters of the system as input. When possible, we assume that the intrinsic properties of each point source are known. For instance, for the TTP and TEB scenarios, we use the properties for the star listed in the TIC and extrapolate any unknown properties using the relations discussed in Section 2.3. In addition, we assume zero eccentricity and a fixed orbital period in all scenarios considered, which significantly simplifies the orbital solution of the system.

Second, rather than calculating the global likelihood of a scenario S_j using Equation 4, we do so by maximizing $p(D|\theta_j, S_j)$ using the equation

$$p(D|\theta_j, S_j) \propto \prod \left[-\frac{1}{2} \left(\frac{y_l - f(t_l|\theta_j)}{\sigma_l} \right) \right] \tag{5}$$

where y_l is the flux of the lth data point (which is different for each star, due to the flux ratio scaling), $f(t_l|\theta_j)$ is the flux given by the model for the parameter vector θ_j at the time of the lth data point, and σ_l is the uncertainty in flux of the lth data point. Thus, for some best-fit parameter vector $\theta_{j,\mathrm{best}}$, we define the global likelihood of the jth scenario as

$$\mathcal{L}_j \equiv \max[p(D|\theta_j, S_j)] = p(D|\theta_{j,\mathrm{best}}, S_j). \tag{6}$$

We then define the prior probability of the jth scenario as

$$\pi_j \equiv p(S_j)p(\theta_{j,\mathrm{best}}|S_j) \tag{7}$$

where $p(S_j)$ involves known system properties (e.g., stellar properties and orbital period) and $p(\theta_{i,\mathrm{best}}|S_j)$ involves free parameters that are fit for. By using this method, we are able to use a simple minimization routine to optimize θ_j and calculate $\mathcal{L}_j$ and π_j for each scenario, which is more expedient than the alternative sampling method.

Our models for TP and EB light curves are generated using `batman` (Kreidberg 2015). TPs are modeled assuming the host star contributes all of the flux of the system, and EBs are modeled assuming both the host and the eclipsing star contribute to the flux of the system. For each model light curve, we use quadratic limb darkening coefficients chosen based on the known T_{eff} and $\log g$ of the host star (Claret 2018).

After calculating $\mathcal{L}_j$ and π_j for each scenario, we determine the relative probability of each scenario using the equation

$$\mathcal{P}_j = \frac{\pi_j \mathcal{L}_j}{\sum_j \pi_j \mathcal{L}_j}. \tag{8}$$

Thus, the most probable scenario is that which produces the highest value of $\mathcal{P}_j$.

2.4.1. *Likelihoods*

As is outlined above, the global likelihood of each scenario is calculated by optimizing the parameter vector θ_j and maximizing Equation 5. Here, we describe the components of θ_j for each scenario, which are outlined in Table 1.

For all TP scenarios, θ_j includes the radius of the transiting planet, R_p, as well as the inclination of its orbit, i. These two parameters capture shape of transit (i.e., depth, ingress/egress duration, and duration). For scenarios where there is an unresolved stellar companion, we also include the flux ratio contributed by the companion, f_c, in θ_j in order to account for light curve dilution. For both PTP and STP scenarios, the luminosity of both the primary and secondary are calculated by dividing the reported luminosity of the target according to f_c, and the remaining stellar properties are determined using the relations discussed in Section 2.3. The same method is used to recalculate the stellar properties of the target star in DTP scenarios. However, this cannot

be done for BTP scenarios, as the luminosity of a hypothetical background star cannot be estimated without designating a distance. In this case, we assume the background star is on the main sequence and calculate $\mathcal{L}_j$ for several instances with stellar properties (e.g., $T_{\rm eff,back}$) drawn from our spline relations, selecting the instance that maximizes $\mathcal{L}_j$.

For all EB scenarios, θ_j includes the flux ratio contributed by the EB, $f_{\rm EB}$, and the inclination of the EB. Unlike the TP scenarios, we cannot simply fit for the radius of the EB because the inferred properties of the host star change based on how much of the flux originates from the EB. We thus rescale the properties of the assumed host according to the value of $f_{\rm EB}$ for each fit. Aside from this difference, the procedure for calculating $\mathcal{L}_j$ for each scenario is the same as that in the TP scenarios.

2.4.2. *Priors*

The prior probability of each scenario is calculated using the equation

$$\pi_j = f(M_\star)\, p(P_{\rm orb})\, p(R_p)\, p_{\rm c}\, p_{\rm geo} \tag{9}$$

where $f(M_\star)$ is the number of short-period planets/binary companions per star with mass $M_\star$, $p(P_{\rm orb})$ is the probability of having a planet/binary companion with an orbital period $P_{\rm orb}$, $p(R_p)$ is the probability of having a planet/binary companion with radius R_p, $p_{\rm c}$ is the probability that there is an unresolved stellar companion near the star, and $p_{\rm geo}$ is the geometric transit probability. To determine these, we use a combination of relations extrapolated from studies of planet occurrence and stellar multiplicity rates, summarized in Figure 1.

For TP scenarios, we calculate $f(M_\star)$ using a linear relation that is consistent with studies of planet occurrence rates for spectral types FGKM. The relation, shown in Figure 1–a, is chosen such that M dwarfs have roughly two planets per star (Dressing & Charbonneau 2015; Mulders et al. 2015b) and FGK dwarfs have roughly one planet per star (Fressin et al. 2013; Petigura et al. 2013). The linear relation we employ returns an occurrence rate of 0.1 for $M_\star = 1.6\,M_\odot$. Because planetary occurrence rates for stars more massive than this are poorly-constrained, we conservatively assume $f(M_\star) = 0.1$ for $M_\star > 1.6\,M_\odot$.

The analogous function used to calculate $f(M_\star)$ for EB scenarios is shown in Figure 1–d. In this panel, the black solid line is obtained by integrating Equation 23 of Moe & Di Stefano (2017) from $\log P_{\rm orb} = 0$ to $\log P_{\rm orb} = 1.7$. Because this study only considers primary stars with masses down to $\sim M_\odot$, we linearly extrapolate the functional form for $M_\star < M_\odot$ so that they are in rough agreement with the results of Winters et al. (2019), which is the most extensive study of M dwarf multiplicity rates to date. Specifically, we use a linear relation such that $f(M_\star = 0) = 0.65\, f(M_\odot)$, which gives us $f(M_\star) \sim 0.2$ at separations < 50 au and $f(M_\star) \sim 0.1$ at separations > 50 au for M dwarf primaries.

We calculate $p(P_{\rm orb})$ for TP scenarios using a logarithmic relation consistent with the results of studies of planet occurrence as a function of orbital period (e.g., Howard et al. 2012; Dong & Zhu 2013; Petigura et al. 2013; Dressing & Charbonneau 2015; Mulders et al. 2015b), shown in Figure 1–b. In particular, we use this relation to capture the drop off in occurrence below ~ 10 days and the leveling-out of occurrence above ~ 10 days (often modeled as a broken power law; e.g., Mulders et al. 2018) We find $p(P_{\rm orb})$ by integrating over a small portion of the distribution centered at $P_{\rm orb}$:

$$p(P_{\rm orb}) = \frac{\int_{\log P_{\rm orb}-0.1}^{\log P_{\rm orb}+0.1} f(P_{\rm orb}) d\log P_{\rm orb}}{\int_{\log(0.2\,{\rm days})}^{\log(50\,{\rm days})} f(P_{\rm orb}) d\log P_{\rm orb}} \tag{10}$$

where $f(P_{\rm orb})$ is a generic function of $P_{\rm orb}$. To prevent spurious probabilities near the limits of this distribution, we allow for a minimum possible orbital period of 0.2 days and a maximum possible orbital period of 40 days.

We calculate $p(P_{\rm orb})$ for EB scenarios by utilizing data from the Kepler Eclipsing Binary Catalog (KEBC, Kirk et al. 2016).[6] We filter the catalog to only include EBs with $P_{\rm orb} < 50$ days and morphologies (as defined in Matijevič et al. 2012) under 0.8, which eliminates binaries detected due to prominent ellipsoidal variations rather than an eclipse of the primary star. We perform a Gaussian kernel density estimation with a bandwidth of 0.2 to estimate the probability density function (PDF) of the resulting data. We then correct this PDF for the geometric probability of transit so that it is representative of all binaries (not just those that eclipse). Since the data has a high completeness in this period regime after performing this correction (Kirk et al. 2016), we do not correct the PDF any further. This process is displayed in Figure 1–e. Using the corrected PDF, we calculate $p(P_{\rm orb})$ with Equation 10.

The distributions used to calculate for $p(R_p)$ for TP scenarios is shown in Figure 1–c. These logistic-like distributions were selected in order to take into account the high frequency of planets smaller than $\sim 2R_\oplus$, the drop-off in planet occurrence rate around $4R_\oplus$, and the continuous decrease in occurrence rate as a function of R_p for planets above $10R_\oplus$ (e.g., Howard et al. 2012; Fressin et al. 2013; Petigura et al. 2013; Mulders et al.

[6] http://keplerebs.villanova.edu/

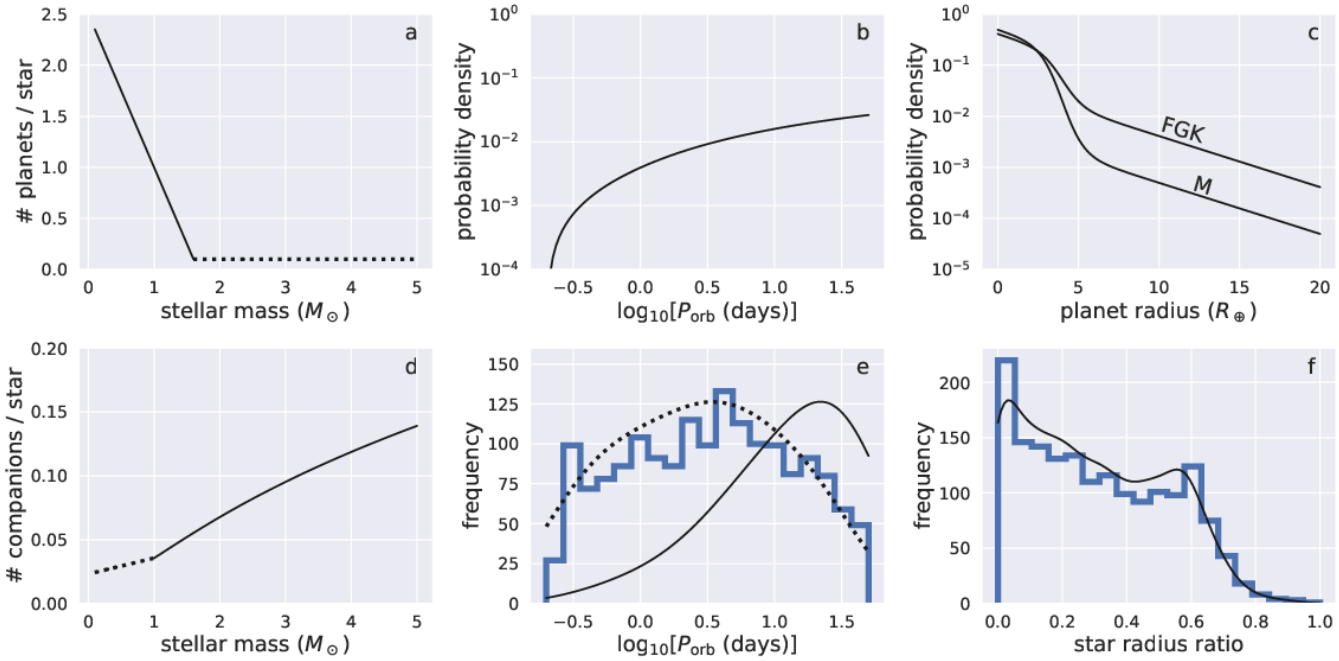

Figure 1. Visualization of the functions used to determine the prior probability of each scenario. a) The number of planets with $P_{\rm orb} < 50$ days per star as a function of $M_\star$. The function for planets around stars with $M_\star < 1.6\,M_\odot$ (black solid line) was chosen to capture the higher planet occurrence rate around stars with lower mass in this $P_{\rm orb}$ regime, while the function for planets around stars with $M_\star > 1.6\,M_\odot$ was chosen to capture our ignorance of planet occurrence rate for main sequence stars more massive than F dwarfs. b) The PDF for planets with $R_p < 20\ R_\oplus$ as a function of $P_{\rm orb}$. c) The PDF for planets with $P_{\rm orb} < 50$ days as a function of R_p for FGK and M dwarfs. d) The number of bound stellar companions with $P_{\rm orb} < 50$ days as a function of $M_\star$. The function for $M_\star \geq M_\odot$ (black solid line) was obtained by integrating Equation 23 of Moe & Di Stefano (2017) and the function for $M_\star < M_\odot$ (black dotted line) is a linear extrapolation based on the results of Winters et al. (2019). e) The $P_{\rm orb}$ distribution of eclipsing binaries with $P_{\rm orb} < 50$ days from the Kepler Eclipsing Binary Catalog (blue histogram), the estimate of the corresponding PDF obtained using a Gaussian KDE (black dotted line, scaled), and the same PDF corrected for geometric transit probability (black solid line, scaled). f) The $R_p/R_\star$ distribution of eclipsing binaries with $P_{\rm orb} < 50$ days from the Kepler Eclipsing Binary Catalog (blue histogram) and the estimate of the corresponding PDF obtained using a Gaussian KDE (black solid line, scaled).

2018). We also use different distributions for M dwarf and FGK dwarf host stars, as the former is known to have a higher occurrence rate of rocky planets and a lower occurrence rate of giant planets (Mulders et al. 2015a). We again calculate this prior probability by integrating over part of the distribution centered at R_p:

$$p(R_p) = \frac{\int_{R_p - x}^{R_p + x} f(R_p) dR_p}{\int_{R_{p,\rm min}}^{R_{p,\rm max}} f(R_p) dR_p} \tag{11}$$

where $f(R_p)$ is a generic function of R_p, $R_{p,\rm min} = 0.5 R_\oplus$, $R_{p,\rm max} = 19.5 R_\oplus$, and $x = 0.5 R_\oplus$.

The PDF used to calculate $p(R_p)$ for EB scenarios is generated in the same way as that made for $p(P_{\rm orb})$, except this time we perform the operation on the distribution of radius ratios (i.e., secondary radius to primary radius). This is displayed in Figure 1–f. We generate this PDF separately for each star such that the minimum possible secondary radius is $0.1 R_\odot$. For each star of size $R_\star$, we calculate $p(R_p)$ using Equation 11 with $R_{p,\rm min} = 0.1 R_\odot$, $R_{p,\rm max} = R_\star$, and $x = (R_\star - 0.1 R_\odot)/40$ (chosen such that the fraction of the PDF integrated over is always the same as that in the TP scenario).[7]

The term $p_{\rm c}$ takes into account the probability of the presence of a bound unresolved stellar companion, $p_{\rm b}$, and an unbound unresolved stellar companion, $p_{\rm u}$. We determine each of these components using the angular separation beyond which we can rule out the existence of an unresolved star at the maximum magnitude difference allowed for another star to produce the observed transit. By default, the value of this separation is set to $2\farcs2$ (Brown et al. 2018), but it can be made arbitrarily small by the user. To find $p_{\rm b}$, we use the mass and parallax of the star to convert this separation into the maximum orbital period of an unresolved secondary,

[7] It should be noted that the KEBC only includes a statistical sample of EBs for FGK stars. We nonetheless assume these distributions in $P_{\rm orb}$ and R_p also apply to OBAM stars.

Table 3. Scenario Probabilities for TOI 465.01

Scenario	$M_\star$ ($M_\odot$)	$R_\star$ ($R_\odot$)	$T_{\rm eff}$ (K)	$L_\star$ ($L_\odot$)	$f_{\rm c}$	i (deg)	R_p ($R_\oplus$)	$\ln \mathcal{L}_j$ [a]	$\ln \pi_j$ 2″.2/0″.85	$\mathcal{P}_j$ 2″.2/0″.85
TTP	0.811	0.847	4936	0.384	0.00	87.41	6.47	-0.10	-9.60/-9.55	0.64/0.69
TEB	0.816	0.840	4953	0.383	0.00	85.40	10.92	-889.76	-11.72/-11.66	<0.01/<0.01
PTP	0.807	0.831	4920	0.365	0.05	87.59	6.49	0.00	-10.47/-10.61	0.30/0.26
PEB	0.700	0.730	4466	0.191	0.50	86.25	10.92	-737.75	-12.72/12.86	<0.01/<0.01
STP	0.701	0.731	4470	0.192	0.50	88.60	7.72	-1.33	-10.79/-10.93	0.06/0.05
SEB	0.626	0.644	4000	0.096	0.25	89.54	10.92	-159.69	-12.85/-12.99	<0.01/<0.01
DTP	0.807	0.831	4920	0.365	0.05	87.59	6.49	0.00	-14.93/-17.23	<0.01/<0.01
DEB	0.700	0.730	4466	0.191	0.50	86.25	10.92	-737.75	-17.12/-19.43	<0.01/<0.01
BTP	0.707	0.736	4500	0.200	0.50	88.53	7.79	-1.44	-15.20/-17.51	<0.01/<0.01
BEB	0.706	0.736	4496	0.199	0.25	89.35	10.92	-4.30	-17.09/-19.40	<0.01/<0.01
TIC [b]	$0.811^{+0.103}_{-0.103}$	$0.847^{+0.055}_{-0.055}$	4936^{+123}_{-123}	$0.384^{+0.013}_{-0.013}$						
WASP-156b [c]	$0.842^{+0.052}_{-0.052}$	$0.76^{+0.03}_{-0.03}$	4910^{+61}_{-61}			$89.1^{+0.6}_{-0.9}$	$5.72^{+0.22}_{-0.22}$			

[a] The values of $\ln \mathcal{L}_j$ are normalized by the highest value, such that the most-likely scenario has $\ln \mathcal{L}_j = 0$

[b] Star properties from version 8 of the TIC (Stassun et al. 2018).

[c] Best-fit star and planet properties from Demangeon et al. (2018).

$P_{\rm orb,max}$, and generate a relation between secondary frequency and $M_\star$ by integrating Equation 23 of Moe & Di Stefano (2017) from $\log P_{\rm orb} = 0$ to $\log P_{\rm orb,max}$ (similar to how we determine $f(M_\star)$ for EB scenarios). To calculate $p_{\rm u}$, we first use TRILEGAL to generate a population of stars in a 0.1 deg^2 cone centered on the coordinates of the target star. We then count the number of stars in the cone fainter than the target star and divide by the best angular resolution of the target. Finally, we calculate $p_{\rm c}$ for each scenario using following relations:

$$p_{\rm c} = \begin{cases} (1-p_{\rm b})(1-p_{\rm u}) & \text{TTP, TEB} \\ p_{\rm b}(1-p_{\rm u}) & \text{PTP, PEB, STP, SEB} \\ (1-p_{\rm b})p_{\rm u} & \text{DTP, DEB, BTP, BEB.} \end{cases} \quad (12)$$

Lastly, the geometric probability of transit is calculated the same for both TP and EB scenarios:

$$p_{\rm geo} = \frac{R_\star + R_p}{a} \quad (13)$$

where a is the semimajor axis of the transiting object.

3. EXAMPLE

For illustrative purposes we display here each step of the validation procedure. We conduct the procedure on the previously-confirmed TOI 465.01 (WASP-156b, Demangeon et al. 2018), a $\sim 6R_\oplus$ planet orbiting a K dwarf with a 3.8 day period. The host star, which has a *TESS* magnitude of $T = 10.73$ and is located 122 pc away, was observed with a 2-minute cadence in the first year of the *TESS* mission.

We begin by searching for all other stars within 100″ of the target star and identifying those that lie within the aperture used to obtain the light curve. This is shown in Figure 2, where the location of each nearby star relative to the local *TESS* pixels is shown on the left and the corresponding *TESS* image is shown on the right. Next, we use the *TESS* magnitude of each star within the aperture to determine what stars are bright enough to produce a transit with the reported depth. In this case, the target star (center-most star in Figure 2) is the only resolved star in the aperture, so we assume it contributes all of the observed flux. We therefore ignore signal-producing scenarios around nearby sources for the remainder of this analysis, which leaves 10 scenarios to be considered.

Next, we determine the best-fit model parameters for each of the 10 scenarios considered. The results of this step are displayed in Figure 4 and Table 3. Figure 4 shows the best-fit transit models for each scenario compared to the extracted *TESS* light curve, which is scaled depending on the scenario due to the different flux ratios considered during this step. Table 3 shows the numerical values for each of these parameters. These are then used to calculate the likelihood and prior probability of each scenario.

The final step in the procedure is to calculate the relative probability of each scenario using Equation 8. These probabilities are shown in the right-most column of Table 3. From here, we can define a "False Positive Probability" (FPP), given by

$$\text{FPP} = 1 - (\mathcal{P}_{\rm TTP} + \mathcal{P}_{\rm PTP} + \mathcal{P}_{\rm DTP}). \quad (14)$$

This quantity represents the probability that the observed transit is due to something other than a TP

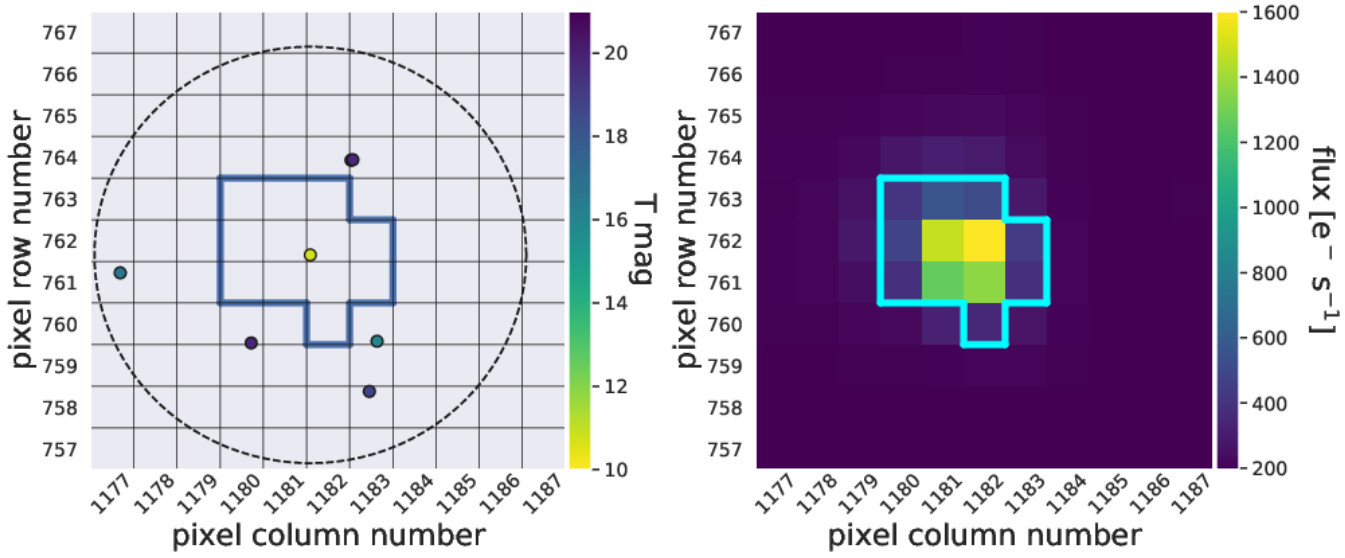

Figure 2. Visualization of TIC querying for TOI 465.01 (TIC 270380593). Left: All stars within 100″ of the target star (the limits of which are approximated by the black dashed line) in *TESS* pixel space. The target star is located in the center pixel. The aperture used to extract the light curve is highlighted in blue. Right: Time-averaged *TESS* image of the same pixels, with the same aperture overlaid.

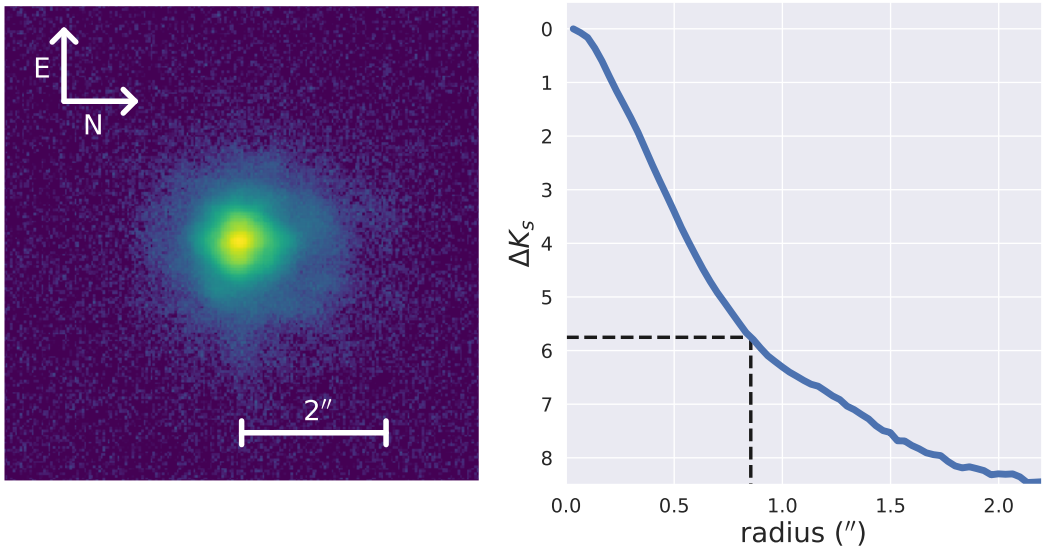

Figure 3. Left: High resolution image of TOI 465 obtained with SHaRCS/ShaneAO in K_s band. Right: Contrast curve of the star (solid line) and separation beyond which we can rule out an unresolved companion with $\Delta K_s = 5.75$ (dashed line).

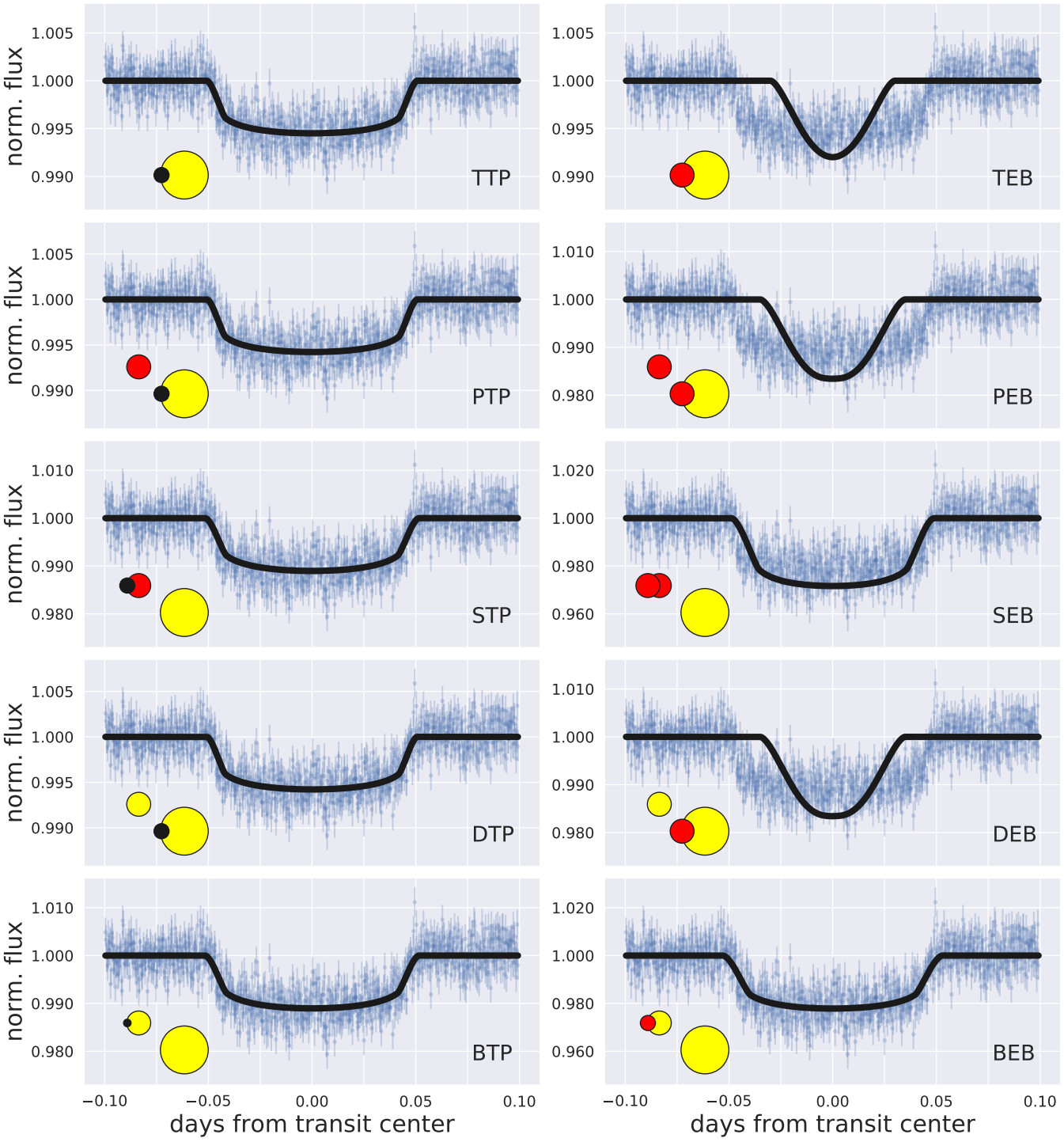

Figure 4. Fit of each transit scenario for TOI 465.01. The purple points are 2-minute cadence *TESS* data, while the black curves are the best-fit light curves. At the bottom-left of each panel is a graphic of the scenario being fit for. In these graphics, yellow and red circles represent main sequence stars of different effective temperatures (where yellow is hotter than red), and black circles represent planets.

around the target star. For this TOI, we find that FPP = 0.06.

The above calculation was done assuming the best angular resolution of the target star is 2″.2. However, if one is able to further constrain the separation beyond which a transit-producing star could exist, this number can be decreased tt new separation. On 2019 July 10, we obtained adaptive-optics-assisted high resolution images of this TOI with SHaRCS/ShaneAO on the Shane 3-meter telescope at Lick Observatory, shown in left-hand panel of Figure 3. These images were reduced using the steps outlined in Hirsch et al. (2019) and Savel et al. (in prep), which we refer the reader to for more information. With these observations, we produce a contrast curve to constrain this separation. Because this system has a transit depth of ∼5000 ppm, the maximum *TESS* magnitude difference of an unresolved companion that can produce this transit is $\Delta T = 2.5\log_{10}(0.005) = -5.75$. Using the contrast curve in the right panel of Figure 3, we are able to rule out companions brighter than this beyond a radius of 0″.85 from the target star.[8]

To show how this changes the results of our tool, we repeat the calculation with this constraint applied. The impact that this follow-up has on the probability of each scenario is shown in Table 3, which now yields FPP = 0.05. The most notable impact this constraint has on the results appears in the prior probabilities of the DTP, DEB, BTP, and BEB scenarios, which decrease by several orders of magnitude.

4. PERFORMANCE ANALYSIS

4.1. *2-minute Cadence Data*

To evaluate the performance of our validation procedure, we run it on TOIs identified by the NASA Science Processing Operations Center (SPOC) pipeline (Jenkins et al. 2016). We use information from the *TESS* Follow-up Observation Program (TFOP) website[9] and 2-minute cadence light curves extracted with simple aperture photometry from MAST[10] to generate phase-folded light curves for input into our algorithm. In order to recreate the conditions under which one would use this tool to vet new TOIs, we only use data from the first sector in which each TOI is observed. Because our tool requires as input extracted *TESS* light curves and their corresponding apertures, we omit TOIs identified by the MIT Quick Look Pipeline, which do not have light curve files containing this information. However, we plan to conduct a full validation analysis of all TOIs from both pipelines in the future.

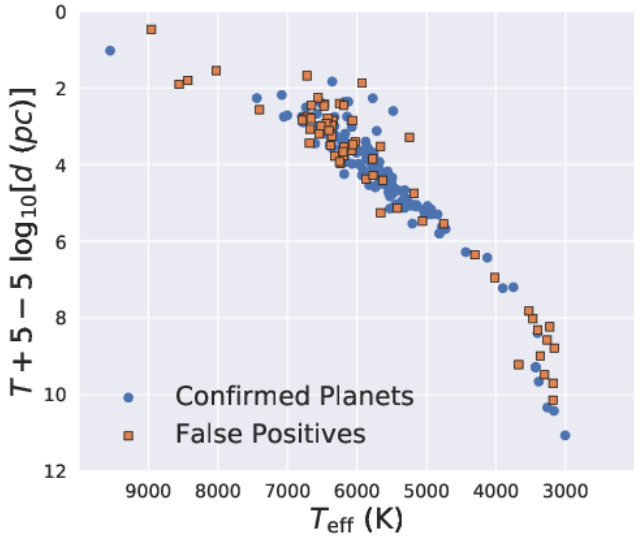

Figure 5. Host properties of TOIs used in our performance analysis. Hosts of TOIs designated as false positives and confirmed planets by TFOP are shown as red squares and blue circles, respectively.

In order to have a ground truth with which to compare the results of our algorithm, we restrict our sample of TOIs to those that have been designated as confirmed planets (CPs) and those that have been designated as false positives (FPs) by the TFOP. We also discard TOIs that have been designated FPs due to instrumental false alarms (which our tool does not test for), TOIs with host stars that display signs of having evolved off of the main sequence, and TOIs for which we were unable to feasibly recover a convincing transit with the purported orbital parameters. This leaves 213 TOIs in total, 149 of which are confirmed planets and 64 of which are false positives. The host properties of these TOIs are displayed in Figure 5.

After generating light curves for these TOIs, we calculate the FPP for each. The results of these calculations are shown in the left-hand column of Figure 6. We see that when a TOI is assigned a FPP < 0.05, it is typically categorized as a CP. However, there is a clear degeneracy between CPs and FPs for TOIs assigned a FPP > 0.95. To determine the origin of this degeneracy, we split our dataset into two groups based on the best-fit radius of the transiting object from the TTP scenario (i.e., in the absence of an unresolved stellar companion). We divide the data into "giant" and "small" TOIs at $R_p = 8R_\oplus$, which corresponds roughly to the minimum radius of a brown dwarf (Sorahana et al. 2013). This radius has been used as an upper limit in the size of objects that

[8] We assume in this calculation that $\Delta T \approx \Delta K_s$.

[9] https://exofop.ipac.caltech.edu/tess/index.php

[10] https://archive.stsci.edu/missions-and-data/transiting-exoplanet-survey-satellite-tess

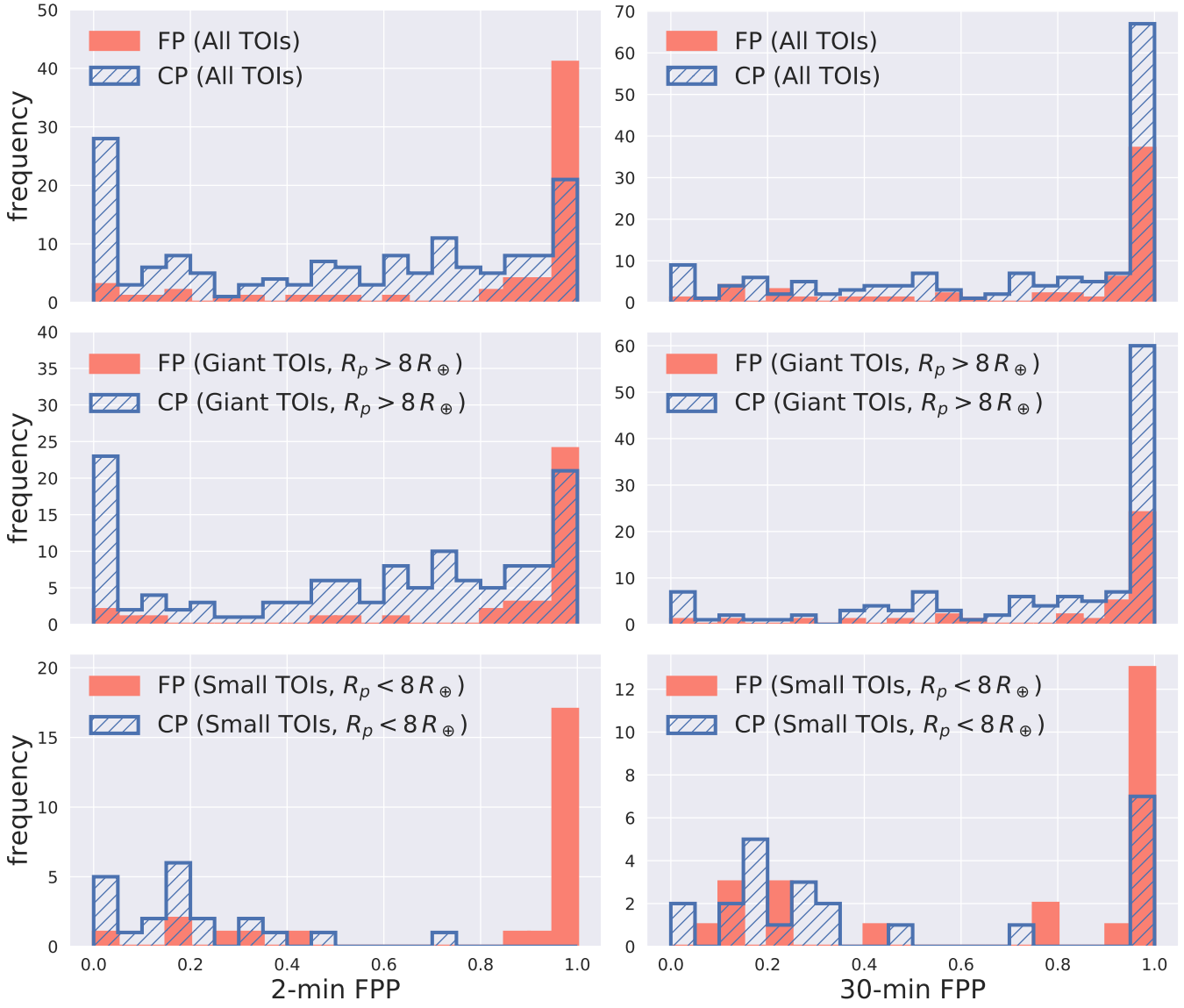

Figure 6. (Left) Histograms of FPPs calculated for 213 TOIs using 2-minute cadence light curves. When using 2-minute data, FPP is a strong predictor of TFOP disposition for small TOIs, and is a strong predictor of TFOP disposition for giant TOIs when FPP < 0.05. (Right) Histograms of FPPs calculated for the same 213 TOIs using 30-minute cadence light curves. Using 30-minute data, FPP is still a strong predictor of TFOP disposition for small TOIs (albeit weaker than it is when using 2-minute data), but is a weak predictor of TFOP disposition for giant TOIs.

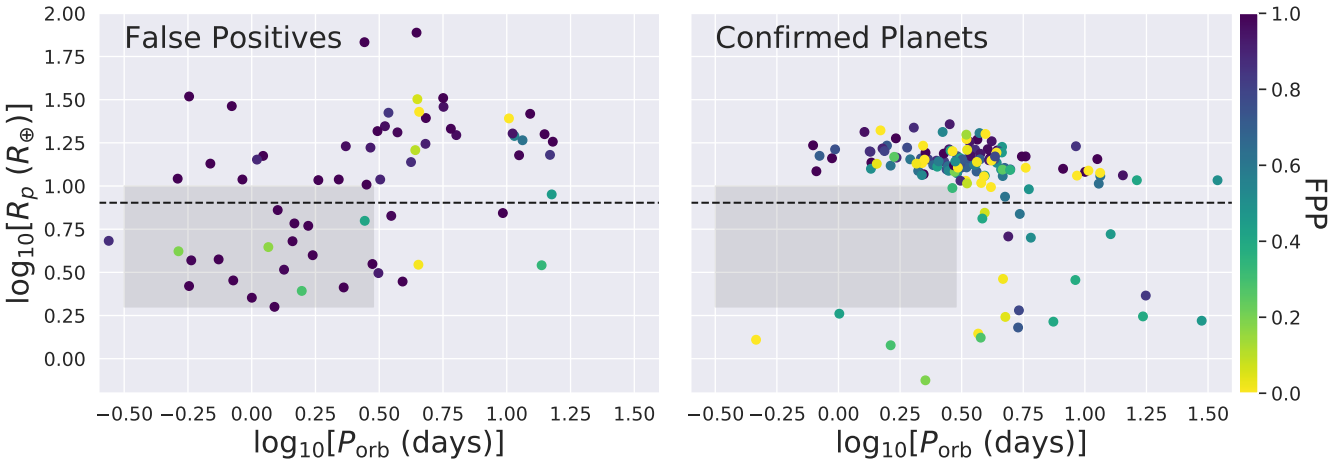

Figure 7. Best-fit radius versus orbital period for all of the TOIs in our sample using 2-minute cadence light curves. FPs are shown on the left and CPs are shown on the right. Color shows FPP as calculated by our tool, where darker points are more likely to be FPs. The black dashed line indicates the radius ($8R_\oplus$) where we split the sample. The location of the sub-Jovian desert is given by the gray rectangles, where there are several FPs and no CPs.

can be validated in past validation studies (Mayo et al. 2018), due to the fact that that giant planets, brown dwarfs, and low-mass stars are typically indistinguishable based on radius alone. After doing this, the degeneracy appears to be contained to the subsample of TOIs with $R_p > 8R_\oplus$. Overall, the FPP calculated when using a light curve extracted from 2-minute cadence data is a strong predictor of TFOP disposition for small TOIs. Specifically, 20/26 small TOIs with FPP < 0.5 are CPs and 19/20 small TOIs with FPP > 0.5 are FPs. It is also a strong predictor of TFOP disposition for giant TOIs when FPP < 0.05, 23/25 of which are CPs.

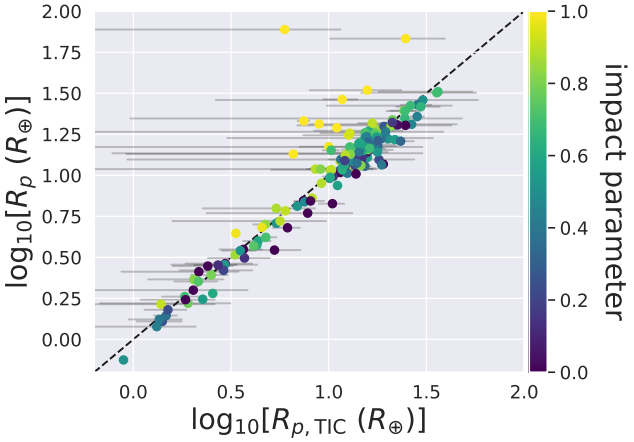

Figure 8. Best-fit radius versus estimated radius for all of the TOIs in our sample using 2-minute cadence light curves. Color shows the best-ft impact parameter of the TOI. TOIs with high inferred impact parameters often have higher best-fit radii due to grazing transits.

For illustrative purposes, we plot our sample of TOIs in R_p–$P_{\rm orb}$ space in Figure 7. One notable feature in this figure is the absence of confirmed planets in the "sub-Jovian desert," a region of the known exoplanet population characterized by a dearth of planets with $P_{\rm orb} < 3$ days and sizes $R_p \sim 2$–$10R_\oplus$ (e.g., Matsakos & Königl 2016; Owen & Lai 2018). Conversely, many false positives are located within this seemingly forbidden region of parameter space. This feature thus may be useful for identifying false positives in future validation studies.

In addition, as a test of the performance of our light curve fitting, we plot in Figure 8 R_p against the estimated planet radius $R_{p,\rm TIC}$, where $R_{p,\rm TIC}$ is calculated using only the reported transit depth of the TOI and the value of $R_\star$ from the TIC. We see that the radii determined from our fitting routine are typically in agreement with the values of $R_{p,\rm TIC}$, except in cases where the best-fit transit has a high impact parameter (i.e., it is a grazing transit).

4.2. *30-minute Cadence Data*

One might expect our code to have a more difficult time distinguishing CPs from FPs when using data with a longer cadence, as they would yield fewer points with which to characterize the shape of the transit. To test this, we also run our code on 30-minute cadence light curves of the same TOIs. We use `eleanor` (Feinstein et al. 2019) to extract these light curves from *TESS* Full Frame Images with the same sectors and apertures used to obtain the 2-minute cadence light curves.

The results of these calculations are shown in the right-hand column of Figure 6. In comparison with the FPPs obtained with 2-minute cadence data, the FPPs obtained using 30-minute cadence data are less corre-

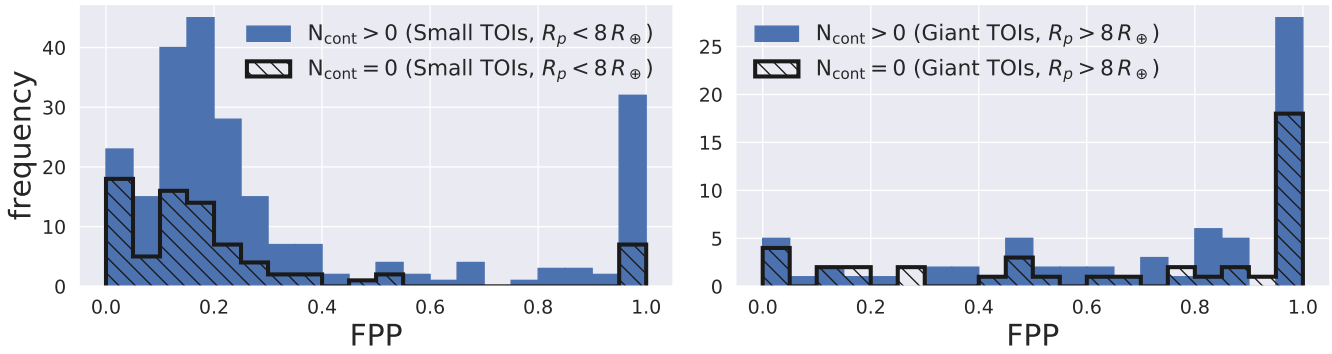

Figure 9. FPP distributions for small planet candidates (left) and giant planet candidates (right). TOIs with no bright contaminants in the aperture that can produce the observed transit ($N_{cont} = 0$) are shown separately from those with at least one of such bright contaminants ($N_{cont} > 0$).

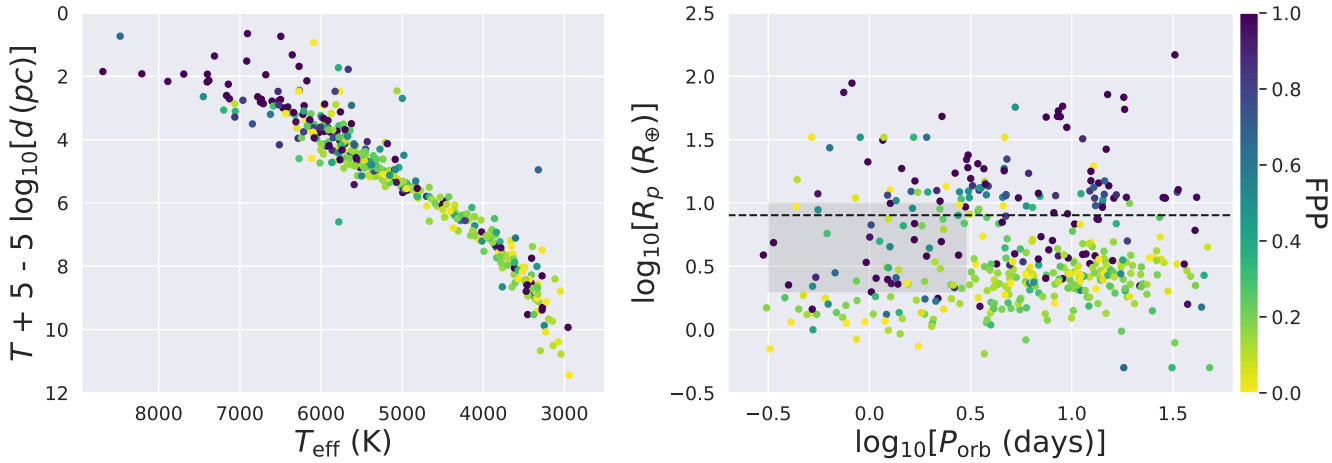

Figure 10. Left: Host properties for each of the 424 TOIs examined. Right: Best-fit planet radius versus orbital period for each of the 424 TOIs examined. The black dashed line indicates the dividing radius ($8R_\oplus$) between small and giant TOIs. The location of the sub-Jovian desert is given by the gray rectangle. In both panels, color indicates FPP, where brighter points have a lower FPP than darker points. Small TOIs inside the desert tend to have higher FPPs than those outside the desert.

lated to their respective TFOP dispositions. The algorithm is generally unable to correctly classify TOIs with $R_p > 8R_\oplus$, and tends to favor high FPPs. However, the tool still performs fairly well for TOIs with $R_p < 8R_\oplus$. For small TOIs, 16/24 TOIs with FPP < 0.5 are CPs, and 16/24 TOIs with FPP > 0.5 are FPs. Thus, FPP can still be used as an indicator of TFOP disposition for small TOIs when using 30-minute cadence data.

5. RESULTS

We apply our code to 424 SPOC TOIs observed in sectors 1–17 that have neither been confirmed as bona fide planets nor rejected as false positives by TFOP. These TOIs were again selected based on our ability to recover a clear transit in their SAP light curves and based on evidence of host star evolution off the main sequence (see Section 4). The results of these calculations are displayed in Figures 9 and 10. More details of these results for each TOI are available in a machine-readable table.

Figure 9 displays the distributions of FPPs for small and giant planet candidates. In order to highlight the effect that bright contaminants (i.e., additional stars in the aperture that are bright enough to produce the observed transit) have on this calculation, we show separate distributions for TOIs with no contaminants and TOIs with at least one contaminant. For small candidates, we identify 262 TOIs with FPP < 0.05 (41 of which have FPP < 0.05) and 61 TOIs with FPP > 0.5 (39 of which have FPP > 0.95). For giant candidates, we identify 9 TOIs with FPP < 0.05 and 102 TOIs with FPP > 0.95.

In Figure 10, we show the host and planet properties for each TOI. In general, low values of FPP are favored for smaller TOIs around cooler stars. In addition, we again see that small TOIs located in the sub-

Jovain desert tend to have higher FPP values compared to other small TOIs with longer orbital periods.

6. DISCUSSION

To gain a better understanding of where our tool is most effective, we provide in Table 4 the probabilities of various FP scenarios for each of the 213 TOIs used in Section 4 (full version available in machine-readable table). In this table, we define three new quantities:

- $\mathcal{P}_{\rm TFP} = \mathcal{P}_{\rm TEB} + \mathcal{P}_{\rm PEB} + \mathcal{P}_{\rm DEB}$ (TFP = "Target False Positive")
- $\mathcal{P}_{\rm CFP} = \mathcal{P}_{\rm STP} + \mathcal{P}_{\rm SEB} + \mathcal{P}_{\rm BTP} + \mathcal{P}_{\rm BEB}$ (CFP = "Companion False Positive")
- $\mathcal{P}_{\rm NFP} = \mathcal{P}_{\rm NTP} + \mathcal{P}_{\rm NEB}$ (NFP = "Nearby False Positive").

In short, $\mathcal{P}_{\rm TFP}$ represents the probability that the observed signal is a FP originating from the target star, $\mathcal{P}_{\rm CFP}$ represents the probability that the observed signal is a FP originating from an unresolved companion, $\mathcal{P}_{\rm NFP}$ represents the probability that the observed signal is a FP originating from a nearby star in the aperture. These probabilities are shown for both 2-minute data and 30-minute data. Table 5 contains the same probabilites for the 424 TOIs examined in Section 5 (full version available in machine-readable table).

According to Table 4, our tool is most effective at identifying small planet candidates that are actually NFPs or CFPs. When working with 2-minute data, we find 13 small TOIs with $\mathcal{P}_{\rm NFP} > 0.5$ and 6 small TOIs with $\mathcal{P}_{\rm CFP} > 0.5$, which accounts for 19/25 small planets that were rejected as false positives. This indicates that the tool is generally able to recognize when the transit-like event is coming from a star other than the target star.

Referring back to Figure 9, we see that most of the small TOIs with high FPPs have multiple stars in their apertures bright enough to produce the observed transit. Upon closer examination of these results, of the 52 small TOIs with FPP > 0.5 and $\rm N_{cont} > 0$, 33 have NFP as the most probable scenario and 19 have CFP as the most probable scenario. That said, it is likely that the transits for these TOIs do not originate from their respective target stars.

Given this strength, we believe that `triceratops` in its current form can best be utilized as a quick vetting tool for small planet candidates. The tool would be particularly useful when used on faint stars in crowded fields where transit signals could originate from more than just the target star. In these cases, `triceratops` can rule out TOIs that are likely to be NFPs and identify those with the highest probabilities of being bona fide planets. TOIs that pass this initial vetting can be prioritized by follow-up observation programs, which can obtain high resolution images and spectra to rule out unresolved companions and confirm the planetary nature of the candidate.

Our tool can also be combined with other vetting tools to provide more robust validation analyses. As of now, `triceratops` is the only validation tool compatible with *TESS* data that models transits from nearby contaminant stars. Seeing as identifying FPs due to nearby stars is one of the strengths of our tool, it can be used as a first step in such an analysis. For example, one could use `triceratops` to find small TOIs with low probabilities of being NFPs and then use tools like `vespa` and `dave` (Kostov et al. 2019) to further constrain the FPP of the planet candidate around the target star. Additionally, comparing the results of several tools would allow one to build a stronger statistical argument for or against the existence of a planet.

To improve the utility of `triceratops`, we plan on adding features that will make the procedure more efficient and robust. First, we will add a feature that searches for centroid shifts during transit to constrain the probability of NFPs. Second, we will add a module that compares the depths of even-numbered transits with those of odd-numbered transits to quantify the chance that one is really the secondary transit of an eclipsing binary pair with twice the orbital period. In addition to this, we will implement more physically accurate eclipsing binary models that take into account secondary transits and ellipsoidal variations. Third, we will improve our priors by expanding to more dimensions that affect planet occurrence rates, such as host metallicity and whether there are other known planets in the system. Fourth, we will make our tool compatible with additional constraints from follow-up observations. For example, we will allow users to rule out unresolved companions below a certain $\Delta T_{\rm eff}$ based on evidence of double-lined spectroscopic binaries.

7. CONCLUSIONS

We present a new tool, `triceratops`, designed for rapid validation of *TESS* Objects of Interest. Using a Bayesian framework that combines transit shape and priors specific to the stars and scenarios being tested, this procedure calculates the probabilities of various transit-producing scenarios for a given TOI in order to provide a false positive probability (FPP). Our tool is also able to fold in information from follow-up observations as additional constraint in these calculations.

We test our tool on 213 TOIs that have been designated as either confirmed planets or astrophysical false

positives by members of the *TESS* Observation Follow-up Program based on follow-up observations. We find that it is able to predict this designation most often when applied to small TOIs ($R_p < 8R_\oplus$) using high-cadence (2-minute) observations. It is also able to correctly identify giant TOIs ($R_p > 8R_\oplus$) with high-cadence observations as bona fide planets when FPP < 0.05. Lastly, we find that our tool is proficient at correctly identifying false positive scenarios where the transit originates from a different, nearby star.

We apply our tool to 424 TOIs with 2-minute cadence observations that have not yet been classified as confirmed planets or rejected as false positives. We identify 262 small TOIs with FPP < 0.5 and 61 small planet candidates with > 0.5. We also identify 9 giant planet candidates with FPP < 0.05.

We recommend using `triceratops` to identify TOIs with high probabilities of being bona fide planets and prioritizing these candidates as targets for further vetting via follow-up observations. When used in combination with other vetting tools, such as `vespa` and `dave`, our tool can also be utilized to perform more thorough validation analyses of planet candidates. We hope this tool will be a valuable resource in the search for planets with *TESS*.

ACKNOWLEDGMENTS

We acknowledge support from the NASA *TESS* Guest Investigator Program through Grant 80NSSC18K1583. We thank Timothy D Morton, Stephen T Bryson, Jack J Lissauer, and Arjun Savel for helpful conversations that improved this paper. We also thank the *TESS* follow-up community for making this work possible through their efforts to vet planet candidates.

REFERENCES

Alonso, R., Brown, T. M., Torres, G., et al. 2004, The Astrophysical Journal Letters, 613, L153

Brown, A., Vallenari, A., Prusti, T., et al. 2018, Astronomy & astrophysics, 616, A1

Burke, C. J., Christiansen, J. L., Mullally, F., et al. 2015, The Astrophysical Journal, 809, 8

Casagrande, L., Flynn, C., & Bessell, M. 2008, Monthly Notices of the Royal Astronomical Society, 389, 585

Claret, A. 2018, Astronomy & Astrophysics, 618, A20

Coughlin, J. L., Thompson, S. E., Bryson, S. T., et al. 2014, The Astronomical Journal, 147, 119

Crossfield, I. J., Ciardi, D. R., Petigura, E. A., et al. 2016, The Astrophysical Journal Supplement Series, 226, 7

Demangeon, O. D., Faedi, F., Hébrard, G., et al. 2018, Astronomy & Astrophysics, 610, A63

Díaz, R. F., Almenara, J. M., Santerne, A., et al. 2014, Monthly Notices of the Royal Astronomical Society, 441, 983

Dong, S., & Zhu, Z. 2013, The Astrophysical Journal, 778, 53

Dressing, C. D., & Charbonneau, D. 2013, The Astrophysical Journal, 767, 95

—. 2015, The Astrophysical Journal, 807, 45

Errmann, R., Torres, G., Schmidt, T. O., et al. 2014, Astronomische Nachrichten, 335, 345

Feinstein, A. D., Montet, B. T., Foreman-Mackey, D., et al. 2019, arXiv preprint arXiv:1903.09152

Fressin, F., Torres, G., Charbonneau, D., et al. 2013, The Astrophysical Journal, 766, 81

Fulton, B. J., Petigura, E. A., Howard, A. W., et al. 2017, The Astronomical Journal, 154, 109

Giacalone, S., Matsakos, T., & Königl, A. 2017, The Astronomical Journal, 154, 192

Ginsburg, A., Sipőcz, B. M., Brasseur, C., et al. 2019, The Astronomical Journal, 157, 98

Girardi, L., Groenewegen, M., Hatziminaoglou, E., & Da Costa, L. 2005, Astronomy & Astrophysics, 436, 895

Hirsch, L. A., Ciardi, D. R., Howard, A. W., et al. 2019, The Astrophysical Journal, 878, 50

Howard, A. W., Marcy, G. W., Bryson, S. T., et al. 2012, The Astrophysical Journal Supplement Series, 201, 15

Huang, Y., Liu, X.-W., Yuan, H.-B., et al. 2015, Monthly Notices of the Royal Astronomical Society, 454, 2863

Jenkins, J. M., Twicken, J. D., McCauliff, S., et al. 2016, in Software and Cyberinfrastructure for Astronomy IV, Vol. 9913, International Society for Optics and Photonics, 99133E

Kirk, B., Conroy, K., Prša, A., et al. 2016, The Astronomical Journal, 151, 68

Königl, A., Giacalone, S., & Matsakos, T. 2017, The Astrophysical Journal Letters, 846, L13

Kostov, V. B., Mullally, S. E., Quintana, E. V., et al. 2019, The Astronomical Journal, 157, 124

Kreidberg, L. 2015, Publications of the Astronomical Society of the Pacific, 127, 1161

Lee, E. J., & Chiang, E. 2017, The Astrophysical Journal, 842, 40

Lopez, E. D., & Fortney, J. J. 2013, The Astrophysical Journal, 776, 2

Matijevič, G., Prša, A., Orosz, J. A., et al. 2012, The Astronomical Journal, 143, 123

Matsakos, T., & Königl, A. 2016, The Astrophysical Journal Letters, 820, L8

Mayo, A. W., Vanderburg, A., Latham, D. W., et al. 2018, The Astronomical Journal, 155, 136

Moe, M., & Di Stefano, R. 2017, The Astrophysical Journal Supplement Series, 230, 15

Morton, T. D. 2012, The Astrophysical Journal, 761, 6

Morton, T. D. 2015, VESPA: False positive probabilities calculator, Astrophysics Source Code Library, , , ascl:1503.011

Muirhead, P. S., Dressing, C. D., Mann, A. W., et al. 2018, The Astronomical Journal, 155, 180

Mulders, G. D., Pascucci, I., & Apai, D. 2015a, The Astrophysical Journal, 814, 130

—. 2015b, The Astrophysical Journal, 798, 112

Mulders, G. D., Pascucci, I., Apai, D., & Ciesla, F. J. 2018, The Astronomical Journal, 156, 24

Owen, J. E., & Lai, D. 2018, Monthly Notices of the Royal Astronomical Society, 479, 5012

Petigura, E. A., Howard, A. W., & Marcy, G. W. 2013, Proceedings of the National Academy of Sciences, 110, 19273

Ricker, G. R., Latham, D., Vanderspek, R., et al. 2010, in Bulletin of the American Astronomical Society, Vol. 42, 459

Sanchis-Ojeda, R., Rappaport, S., Winn, J. N., et al. 2014, The Astrophysical Journal, 787, 47

Santerne, A., Díaz, R., Moutou, C., et al. 2012, Astronomy & Astrophysics, 545, A76

Santerne, A., Díaz, R., Almenara, J.-M., et al. 2015, Monthly Notices of the Royal Astronomical Society, 451, 2337

Savel, A., Dressing, C. D., Hirsch, L. A., et al. in prep

Sorahana, S., Yamamura, I., & Murakami, H. 2013, The Astrophysical Journal, 767, 77

Stassun, K. G., Oelkers, R. J., Pepper, J., et al. 2018, The Astronomical Journal, 156, 102

Torres, G., Andersen, J., & Giménez, A. 2010a, The Astronomy and Astrophysics Review, 18, 67

Torres, G., Konacki, M., Sasselov, D. D., & Jha, S. 2004, The Astrophysical Journal, 614, 979

—. 2005, The Astrophysical Journal, 619, 558

Torres, G., Fressin, F., Batalha, N. M., et al. 2010b, The Astrophysical Journal, 727, 24

Winters, J. G., Henry, T. J., Jao, W.-C., et al. 2019, The Astronomical Journal, 157, 216

Table 4. FPP Calculations for Classified TOIs

TOI	$\mathcal{P}_{\rm TFP}$	$\mathcal{P}_{\rm CFP}$	$\mathcal{P}_{\rm NFP}$	FPP	TFOP Disp.	R_p ($R_\oplus$)
	2m/30m	2m/30m	2m/30m	2m/30m		2m/30m
101.01	0.01/0.78	<0.01/0.06	<0.01/<0.01	0.01/0.84	CP	13.4/15.7
102.01	<0.01/0.01	>0.99/<0.01	–/–	>0.99/0.01	CP	16.1/16.1
103.01	<0.01/0.02	0.78/0.45	–/–	0.78/0.46	CP	13.4/13.8
104.01	>0.99/0.84	<0.01/<0.01	–/–	>0.99/0.84	CP	14.2/14.1
105.01	<0.01/>0.99	<0.01/<0.01	–/–	<0.01/>0.99	CP	13.6/14.0
106.01	0.03/>0.99	0.68/<0.01	<0.01/<0.01	0.71/>0.99	CP	16.0/15.7
107.01	<0.01/0.99	<0.01/<0.01	<0.01/<0.01	<0.01/0.99	CP	20.0/19.9
108.01	0.04/0.22	0.71/0.2	–/–	0.75/0.41	CP	12.1/11.7
109.01	0.02/0.08	0.49/0.3	–/–	0.51/0.37	CP	12.7/11.2
110.01	0.2/0.19	0.61/<0.01	–/–	0.81/0.19	CP	12.8/7.9
			⋮			

Note—TOIs with "–" for a value under $\mathcal{P}_{\rm NFP}$ do not consider NTP or NEB scenarios (i.e., they have no other stars in their apertures capable of producing the observed transit). Table 4 is published in its entirety in the machine-readable format. A portion is shown here for guidance regarding its form and content.

Table 5. FPP Calculations for Unclassified TOIs

TOI	$\mathcal{P}_{\rm TFP}$	$\mathcal{P}_{\rm CFP}$	$\mathcal{P}_{\rm NFP}$	FPP	R_p ($R_\oplus$)	$N_{\rm cont}$
1051.01	<0.01	<0.01	>0.99	>0.99	2.2	1
1052.01	0.03	<0.01	0.1	0.14	3.1	3
1053.01	0.04	<0.01	0.81	0.85	3.4	5
1054.01	<0.01	<0.01	<0.01	<0.01	2.9	1
1055.01	0.04	<0.01	–	0.04	3.4	0
1056.01	0.22	<0.01	<0.01	0.23	2.6	2
1058.01	0.31	<0.01	0.06	0.37	11.8	5
1059.01	>0.99	<0.01	–	>0.99	39.5	0
1060.01	0.14	<0.01	–	0.14	1.2	0
1063.01	0.18	<0.01	–	0.18	2.3	0
			⋮			

Note—TOIs with "–" for a value under $\mathcal{P}_{\rm NFP}$ do not consider NTP or NEB scenarios (i.e., they have no other stars in their apertures capable of producing the observed transit). Table 5 is published in its entirety in the machine-readable format. A portion is shown here for guidance regarding its form and content.

.